Journal of Alloys and Compounds 517 (2012) 118–126

Contents lists available at SciVerse ScienceDirect

Journal of Alloys and Compounds

journal homepage: www.elsevier.com/locate/jallcom

Evolution of microstructure and properties in a new type 2 mm Al–Zn–Mg–Sc–Zr alloy sheet

Ying Deng[a], Zhimin Yin[a,*], Jiaqi Duan[a], Kai Zhao[a], Bei Tang[a], Zhenbo He[b]

[a] School of Materials Science and Engineering, Central South University, Changsha 410083, China
[b] Northeast Light Alloy Co. Ltd., Harbin 150060, China

ARTICLE INFO

Article history:
Received 22 September 2011
Received in revised form 9 December 2011
Accepted 12 December 2011
Available online 21 December 2011

Keywords:
Aluminum alloys
Mechanical properties
Microstructure
Electron microscopy

ABSTRACT

The microstructural and property evolution of a novel Al–Zn–Mg–Sc–Zr sheet during its preparation were investigated in detail by tensile tests and electron microscopy methods. The results show that severe segregation exists in the ingot. After homogenization treatment at 470 °C for 12 h, dissoluble Zn and Mg enriched non-equilibrium phases dissolve into matrix completely and only little indissoluble impurity phases containing Fe and Si elements remain. At the same time, precipitation of nanometer-scaled coherent secondary $Al_3(Sc, Zr)$ particles from a supersaturated solid solution occurs. The proper homogenization process is 470 °C × 12 h. After solution treatment at 470 °C for 1 h, a lot of non-equilibrium $T(Mg_{32}(Al,Zn)_{49})$ phases formed during hot rolling dissolve into matrix. Aged at 120 °C, the precipitates gradually transform from coherent GP zones to semi-coherent η′ phase and incoherent η phase for the duration of aging, exhibiting a typical behavior of aging strengthening. The optimal solution-aging process is solution treated at 470 °C for 1 h, followed by water quenching and then aged at 120 °C for 24 h (peak-aged). Under this condition, the ultimate tensile strength, yield strength and elongation reach 555 ± 2 MPa, 524 ± 4 MPa and 12.3 ± 0.6% respectively. The main strengthening mechanisms of Al–Zn–Mg–Sc–Zr aged sheets are precipitation strengthening derived from η′ precipitates, and dispersion strengthening and sub-grain strengthening caused by coherent secondary $Al_3(Sc, Zr)$ particles.

1. Introduction

7xxx series aluminum alloys are used extensively for structure components in aerospace industry owing to their excellent mechanical properties [1–5]. However, with the development of aerospace technology, it is urgent to develop new aluminum alloys with better performance. Material workers have found that rare-earth elements are of great importance to improve the service performance of Al-based alloys [6–10]. On a per-atom basis, scandium (Sc) has the greatest strengthening effect of any existing alloying addition to Al [11–13]. Moreover, recent researches indicate that additions of minor zirconium to aluminum alloys with scandium enhance positive effect on the set of their operational properties, due to the formation of extremely fine, coherent $Al_3(Sc, Zr)$ particles with $L1_2$ structure, which can substantially inhibit recrystallization and pin dislocations [14–16]. Knipling [17,18] showed that Zr additions provided a secondary strength increase from the precipitation of Zr-enriched outer shells onto the Al_3Sc precipitates. Van Dalen [19] and Booth-Morrison [20] indicated that additions of Zr and Sc improved coarsening resistance of $Al_3(Sc, Zr)$ ($L1_2$) precipitates compared with Al_3Sc ($L1_2$). Wu [21] showed that the finest and densest dispersoid of spherical $Al_3(Sc, Zr)$ particles resulting from the optimum homogenization condition can effectively inhibit recrystallization and resulting in the smallest fraction of recrystallized structure, and hence exhibiting the highest strength after aging treatment in an Al–Zn–Mg–Sc–Zr alloy. Senkov [22] found that the Orowan strengthening from the coherent nanometer-sized $Al_3(Sc, Zr)$ particles provided 40–63% of the yield strength increase relative to the alloy without the nanometer-sized $Al_3(Sc, Zr)$ particles in SSA018 alloy.

New Al–Zn–Mg–Sc–Zr alloy in the high-strength thermally strengthened weldable alloys based on the Al–Zn–Mg system with scandium and zirconium additives is developed by All-Russia Institute of Light Alloys, namely, 01970 and 01975 [21,23]. Between those two alloys, the alloy 01970 contains more Sc additives, achieving higher strength and toughness, better corrosion resistance and welding performance. It belongs to a new generation lightweight structural material [24]. However, less reports of this novel alloy are available, limiting its extensive applications. Therefore, it is highly significant to develop this high performance

* Corresponding author. Tel.: +86 731 88830262; fax: +86 731 88830262.
E-mail address: zmyin@163.com (Z. Yin).

0925-8388/$ – see front matter © 2011 Elsevier B.V. All rights reserved.
doi:10.1016/j.jallcom.2011.12.049

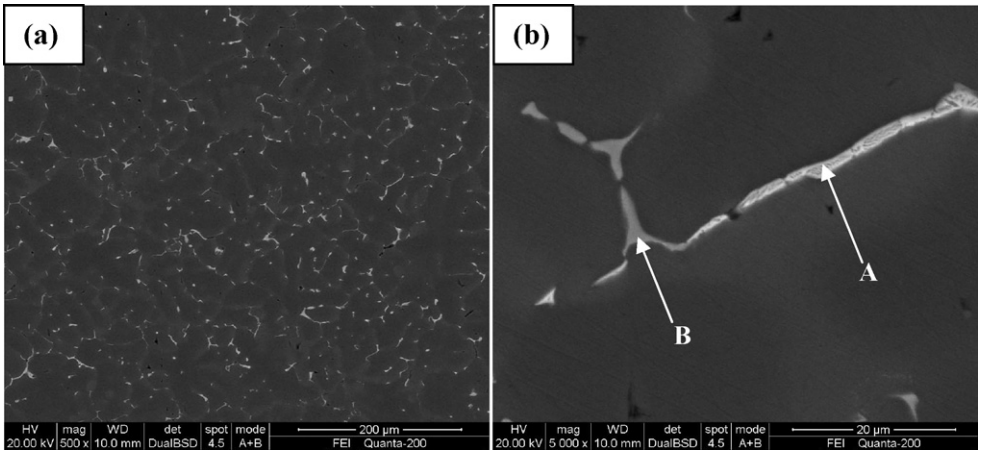

Fig. 1. Back scattered electron images of the as-cast alloy: (a) low magnification and (b) high magnification.

aluminum alloy to meat the requirements of aerospace users as soon as possible. In this paper, we aim to prepare a new type 2 mm Al–Zn–Mg–Sc–Zr alloy sheet with good mechanical properties. Based on this, the microstructural evolution of this sheet during its preparation is investigated systematically. The purpose of this paper is to provide theoretical and experimental basis for engineering design and application of this novel alloy.

2. Material and methods

The semi-continuous ingots, with 172 mm in diameter, were provided by Northeast Light Alloy Co. Ltd. The chemical composition is Al–5.7Zn–1.98Mg–0.33Cu–0.25Sc–0.10Zr–0.18Fe–0.11Si–0.32Mn (wt.%).

According to the upper limit of homogenization temperature obtained from differential scanning calorimetry (DSC) analysis, the suitable homogenization temperature was selected. Materials for hardness and electrical conductivity measurements were cut from ingot with dimension of 25 mm × 25 mm × 6 mm. The specimens were homogenized at selected temperature for different durations in a salt bath furnace. After homogenization treatment, the specimens were quenched in water immediately. The homogenized samples were investigated by hardness and electrical conductivity measurements, and microstructural observations. According to the microstructures and properties of homogenized samples, optimized homogenization parameters were obtained.

After optimal homogenization treatment, the ingots, with dimension of ø172 mm × 70 mm, were annealed at 420 °C for 4 h, then hot rolled to 7 mm thick plates immediately. The hot rolled plates were annealed at 420 °C for 1 h, and cold rolled to 2 mm sheets. The sheets were subjected to solution treatments at 450 °C, 460 °C, 470 °C, 480 °C and 490 °C for 0.5 h, 1 h and 1.5 h respectively, followed by water quenching, and then aged at 100 °C, 110 °C, 120 °C and 130 °C for 10 min–36 h. The solution-aging treated sheets under different conditions were investigated by tensile tests and microstructural observations. According to the microstructures and properties of different solution-aging treated samples, optimized solution-aging process was acquired.

DSC analyses were conducted using a SDT-Q600 differential scanning calorimeter. Samples were heated in an inert flowing atmosphere (N_2) at a constant heating rate of 10 °C/min from 25 to 650 °C. The standard sample is Al_2O_3. Hardness and electrical conductivity measurements were finished on an HW187.5 Brinell's machine and a D60K digital conductivity meter respectively. The mechanical testing utilized transverse orientation (normal to rolling direction) specimens. Tensile properties were performed on a CSS-44100 electronic universal testing machine with 2 mm/min loading speed. Yield strength of the material was identified at 0.2% plastic strain. A minimum of three mechanical tests was performed on each sample, and their statistical scatter determined the measurement errors. All of the experimental errors or uncertainties reported here represent one standard deviation from the mean. Scanning electron microscope (SEM) samples were observed on a Quanta MK2-200 SEM, operating at 20 kV. X-ray diffraction was carried out on a D/max 2500PC diffraction instrument with CuKα_1 radiation. Thin foils for transmission electron microscope (TEM) and high resolution electron microscope (HRTEM) observations were sectioned from the alloys under different conditions. The foils were prepared by double-jet electro-polishing at 20 V in a solution of 30% nitric acid and 70% methanol solution cooled to −30 °C and observed on a TECNAIG^2 20 electron microscope and a JEM-3010 electron microscope respectively, both with an acceleration voltage of 200 kV.

3. Results

3.1. Microstructure of cast alloy

The as-cast microstructures are shown in Fig. 1. The average diameter of grains is about 50 μm. Serious segregation exists in grain boundaries (Fig. 1(a)). Inter-metallic phases in the grain boundaries are presented in Fig. 1(b). According to the energy dispersive X-ray (EDX) analysis, the white secondary phases as shown in Fig. 1(b) A, are enriched in Zn and Mg elements non-equilibrium phases. The grey phases as shown in Fig. 1(b) B are indissoluble impurity phases containing Fe and Mn elements. The EDX results are shown in Table 1. As massive intermediate compounds affect the subsequent processing properties, to ensure the service performance of the alloy, a homogenization treatment is required to eliminate severe segregation in as-cast alloy. Higher temperature increases the possibility of burnt phenomenon. Thus, before homogenization treatment, it is highly necessary to obtain burnt temperature of the ingot.

Fig. 2 gives DSC curve of as-cast Al–Zn–Mg–Sc–Zr alloy. An obvious endothermic peak sited at 478 °C is observed. It illustrates that non-equilibrium phase which starts melting at 475 °C exists in the ingot. Therefore, the upper limit temperature for homogenization treatment is 470 °C.

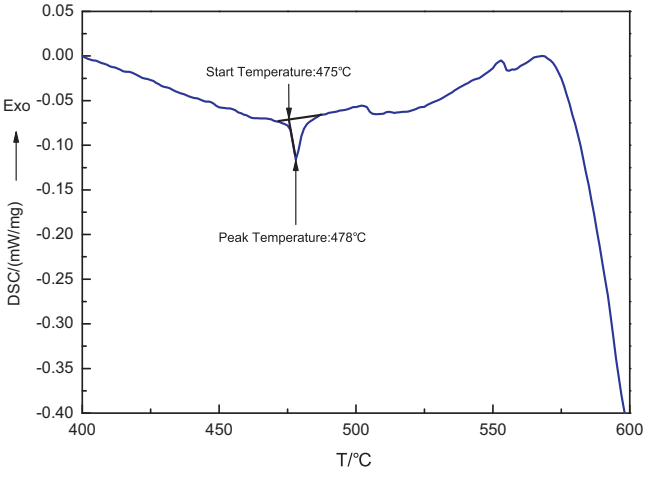

Fig. 2. DSC curve of the as-cast Al–Zn–Mg–Sc–Zr alloy.

Table 1
Chemical composition of the secondary phases in Fig. 1 (in at.%).

Phase	Al	Zn	Mg	Cu	Fe	Si	Mn
A	68.20 ± 0.68	13.07 ± 0.07	15.65 ± 0.11	3.09 ± 0.11	0	0	0
B	79.83 ± 1.88	1.50 ± 0.04	1.29 ± 0.31	0.66 ± 0.01	11.18 ± 1.66	3.81 ± 0.10	1.73 ± 0.08

3.2. Effect of homogenization treatment on as-cast alloy

3.2.1. Effect of homogenization treatment on the hardness and electrical conductivity of as-cast alloy

In order to optimize homogenization time, the curves of hardness and conductivity in the Al–Zn–Mg–Sc–Zr alloy homogenized at 470 °C for different durations were shown in Fig. 3. Hardness increases, but conductivity decreases for the duration of homogenization. After homogenization treatment for 12 h, the hardness and conductivity almost keep constant with the prolongation of homogenization time. This indicates that solvable non-equilibrium phases have mainly dissolved into matrix after homogenizing at 470 °C for 12 h.

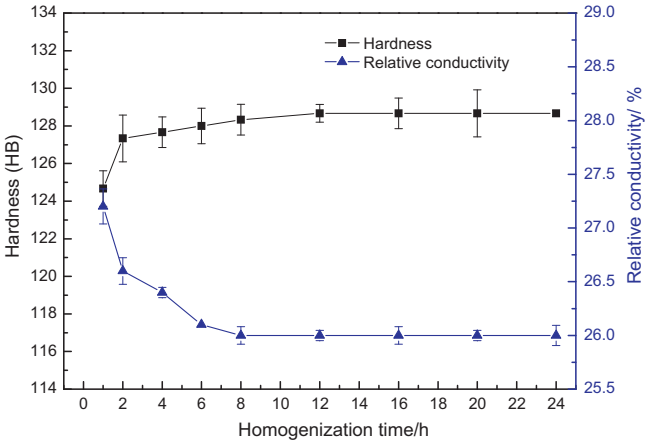

Fig. 3. Curves of the hardness and electrical conductivity in the Al–Zn–Mg–Sc–Zr alloy homogenized at 470 °C.

3.2.2. Effect of homogenization treatment on microstructures of as-cast alloy

The SEM images in Fig. 4 show microstructures of homogenized alloys. After homogenization at 470 °C for 12 h, only little grey phases exist in ingot (Fig. 4(a)). As further prolonging the holding time, no obvious secondary phase dissolution is observed (Fig. 4(b)). The residual phases are magnified in Fig. 4(c). According to the result of EDS analysis, the residual grey phases are indissoluble impurity phases containing Fe, Mn and Si elements. These phases cannot be eliminated by homogenization treatment. Compared with the microstructures of ingot (in Fig. 1(a)), solvable phase primarily dissolves into matrix after homogenization at 470 °C for 12 h. Therefore, the suitable homogenization treatment is 470 °C × 12 h. This is confirmed by the subsequent TEM observation.

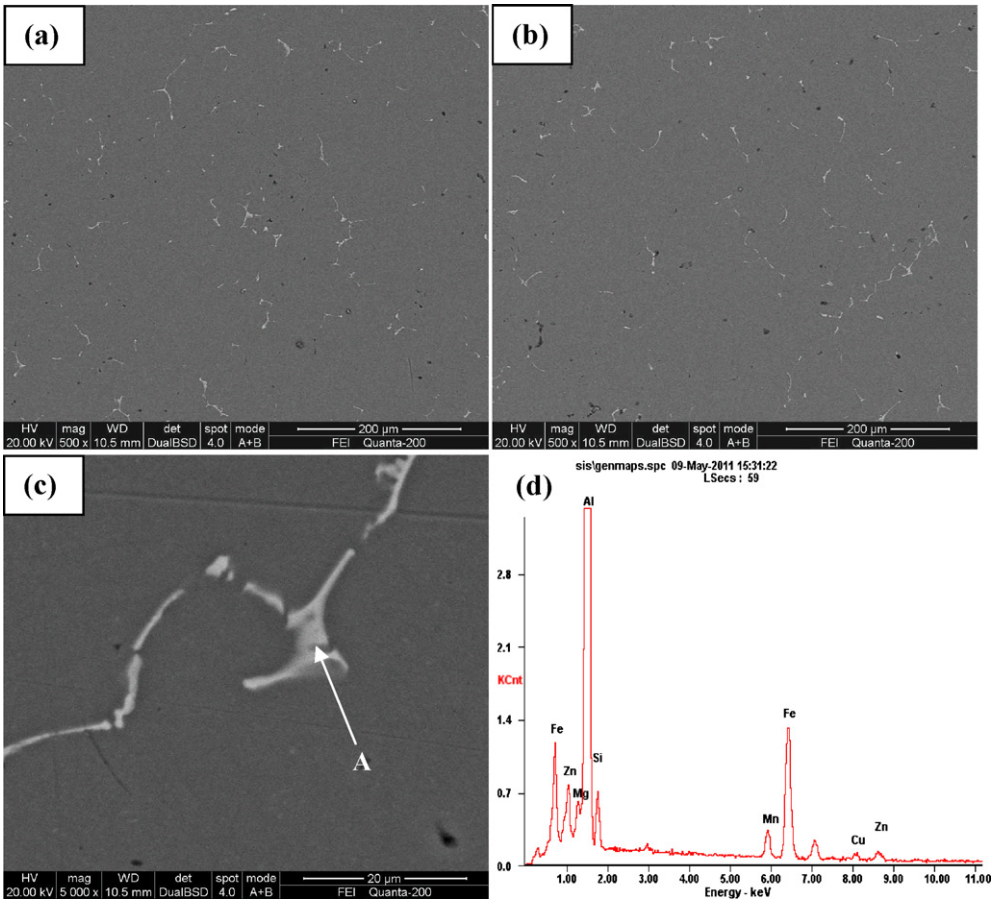

Fig. 4. Back scattered electron images of the alloy homogenized at 470 °C: (a) 12 h, low magnification; (b) 24 h; (c) 12 h, high magnification; (d) EDS patterns of the phase in (c) A.

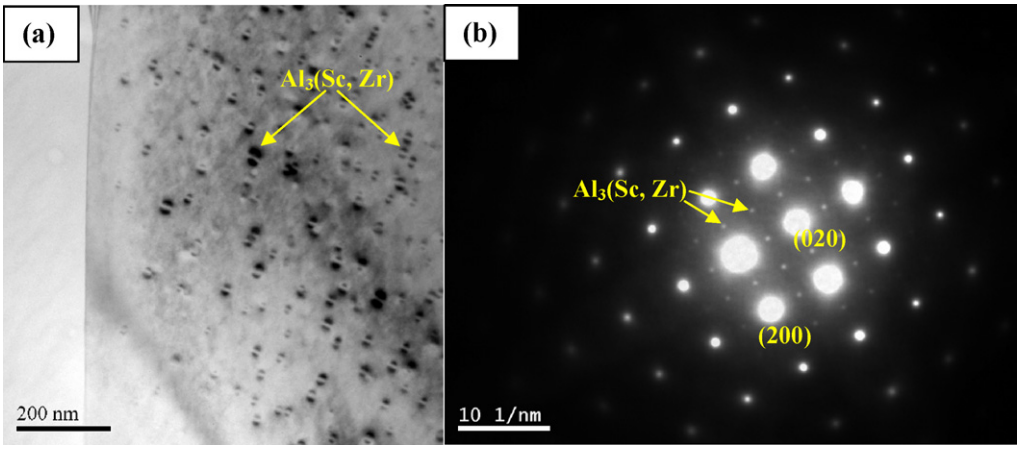

Fig. 5. Microstructures of the alloy homogenized at 470 °C for 12 h: (a) bright image and (b) SAD in $[0\,0\,1]_{Al}$ projection.

The TEM images in Fig. 5 show microstructures of the alloy homogenized at 470 °C for 12 h. The results show that little coarse non-equilibrium phases are observed in the grain and grain boundaries. Besides, dispersive, fine, nanometer-sized, spherical particles precipitate from matrix (Fig. 5(a)). The presence of Ashby-Brown contrast for bright-field images of $Al_3(Sc, Zr)$ particles (Fig. 5(a)), as well as the superstructure reflections like (0 1 0) and (1 1 0) (Fig. 5(b)), confirms that this particle is $Al_3(Sc, Zr)$ particle with an Ll_2 cubic crystal structure, which is coherent with the Al matrix. This is in accordance with the previous reports [17,18,25,26].

3.3. Effect of solution-aging treatment on microstructures and properties of cold-rolled sheets

3.3.1. Burnt temperature of cold-rolled sheet

To obtain the upper temperature of solution treatment, the cold-rolled sheet was used for DSC analysis. Fig. 6 shows DSC curve of cold-rolled Al–Zn–Mg–Sc–Zr sheet. It indicates that low-melting non-equilibrium phase starts to melt at 487 °C and reaches its peak melting temperature at 493 °C. Therefore, the upper limit temperature for solution treatment is 490 °C.

3.3.2. Effect of solution-aging treatment on the tensile properties of cold-rolled sheets

Fig. 7 shows the effect of different solution treatments on mechanical properties of cold-rolled sheets aged at 120 °C for 24 h.

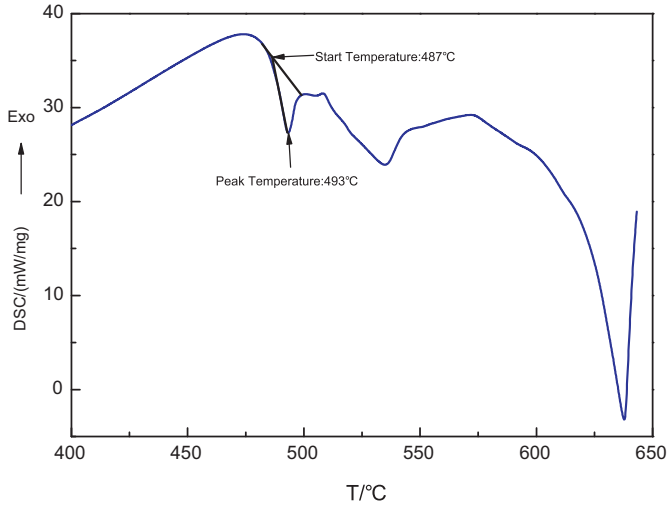

Fig. 6. DSC curve of the cold-rolled Al–Zn–Mg–Sc–Zr sheet.

With increasing solution temperatures, strength and elongation of aged alloys increase firstly and then decrease (Fig. 7(a)). As further prolonging holding time at 470 °C, strength increases firstly and then decreases, and elongation decreases monotonously (Fig. 7(b)). From Fig. 7, it can be concluded that the sheets had best tensile properties after solution at 470 °C for 1 h.

Fig. 8 shows the effect of aging treatment on tensile properties of the sheets after solution treatment at 470 °C for 1 h. The

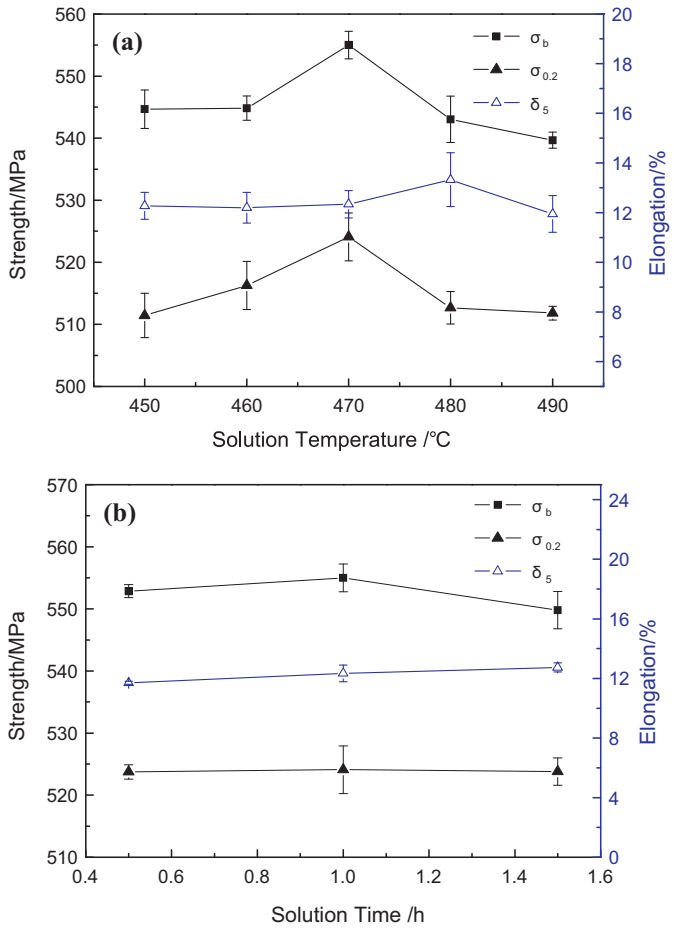

Fig. 7. Effect of solution treatment on mechanical properties of cold-rolled sheets aged at 120 °C/24 h: (a) solution treated at different temperatures for 1 h and (b) solution treated for different time at 470 °C. σ_b, ultimate tensile strength■; $\sigma_{0.2}$, yield strength ▲; δ_5, elongation △.

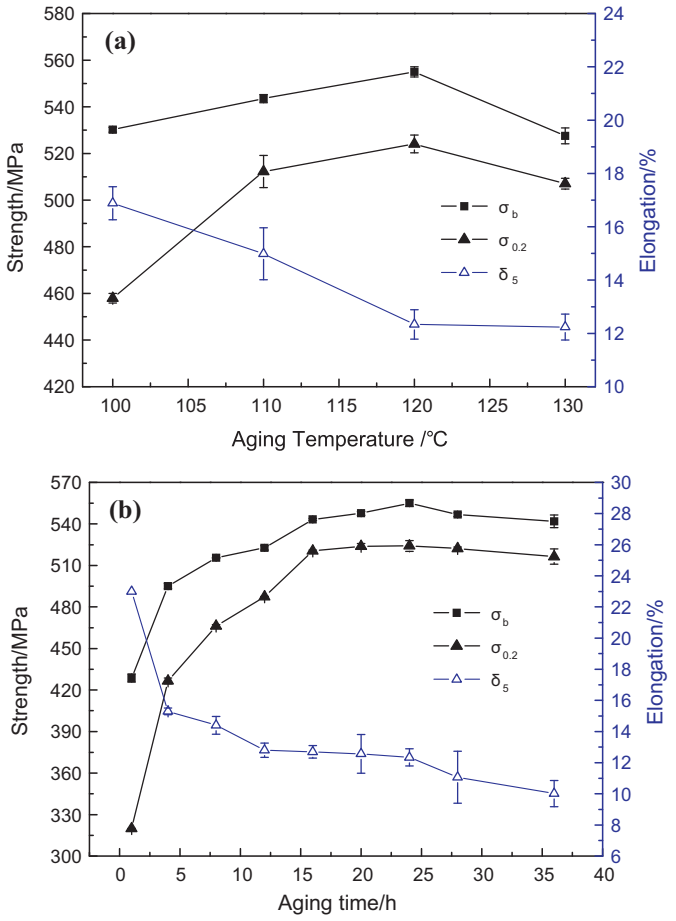

Fig. 8. Effect of aging treatment on the mechanical properties of the sheets after solution treatment at 470 °C/1 h: (a) aged at different temperatures for 24 h and (b) aged for different duration at 120 °C. σ_b, ultimate tensile strength ■; $\sigma_{0.2}$, yield strength ▲; δ_5, elongation △.

tensile property curves of the alloys aged at different temperatures for 24 h are shown in Fig. 8(a). With increasing aging temperatures, strength rises firstly and then decreases, but elongation decreases firstly and then keeps constant. Fig. 8(b) shows tensile properties of the alloy aged at 120 °C, as a function of aging time. It can be seen that the age strengthening effect of the alloy is obvious. In initial stage of aging, the strength rises rapidly. Peak aging is achieved after 24 h of aging. During the over-aging stage, the strength has a little change for the duration of aging time, but the elongation decreases monotonously. Comparatively, the sheets aged at 120 °C for 24 h exhibit better tensile properties. After suitable solution treatment (470 °C × 1 h) and proper aging treatment (120 °C × 24 h), the tensile strength, yield strength and elongation of the sheet reach 555 ± 2 MPa, 524 ± 4 MPa and 12.3 ± 0.6% respectively.

3.3.3. *Effect of solution-aging treatment on microstructures of cold-rolled sheets*

To ensure the best probability of finding the proper solution treatment, the microstructures of cold-rolled sheets solution treated at 470 °C for 1 h were used for SEM, XRD and TEM analyses. SEM microstructures from cold-rolled sheet along the rolling direction and from solution treated alloy are shown in Figs. 9(a) and (b) for comparison. Massive non-equilibrium phases formed during rolling exist in cold-rolled sheets. Those phases can be divided into two kinds. According to the results of EDS analyses, the short rod-like phases as shown in Fig. 9(a) A, are enriched in Zn and Mg elements non-equilibrium phases. The irregular phases as shown in Fig. 9(a) B, are indissoluble impurity phases containing Fe, Si and Mn elements. After solution treatment at 470 °C for 1 h, the Zn and Mg enriched particles are dissolved into matrix completely, and only little impurity phases are remained in solution treated alloy (Fig. 9(b) C). The EDS results are shown in Table 2.

X-ray diffraction patterns of cold-rolled sheet and solution treated alloy are shown in Fig. 10. The phases in cold-rolled sheet are composed of Al(α) matrix and T($Mg_{32}(Al,Zn)_{49}$) phase. After solution treatment at 470 °C for 1 h, T($Mg_{32}(Al,Zn)_{49}$) phase has dissolved into matrix completely. In addition, it can be inferred that the Zn and Mg enriched particles as shown in Fig. 9(a) A are T($Mg_{32}(Al,Zn)_{49}$) phases.

The TEM images in Fig. 11 show microstructures of solution treated sheets. After solution treatment at 470 °C for 1 h, the alloy still remains unrecrystallized, fiber-like structures. The fiber-like structures are made up of micrometer-sized subgrains. Observed through high magnification, numerous, fine, nanometer-sized, spherical $Al_3(Sc, Zr)$ particles are distributed in sub-grain and sub-grain boundaries. Those particles strongly pin sub-grain boundaries, leading to structures maintaining unrecrystallization after rolling and solution treatment. Fig. 11(c) is the selected area diffraction (SAD) pattern of $Al_3(Sc, Zr)$ particles in solution treated samples taken along [0 1 1] zone axes of Al matrix.

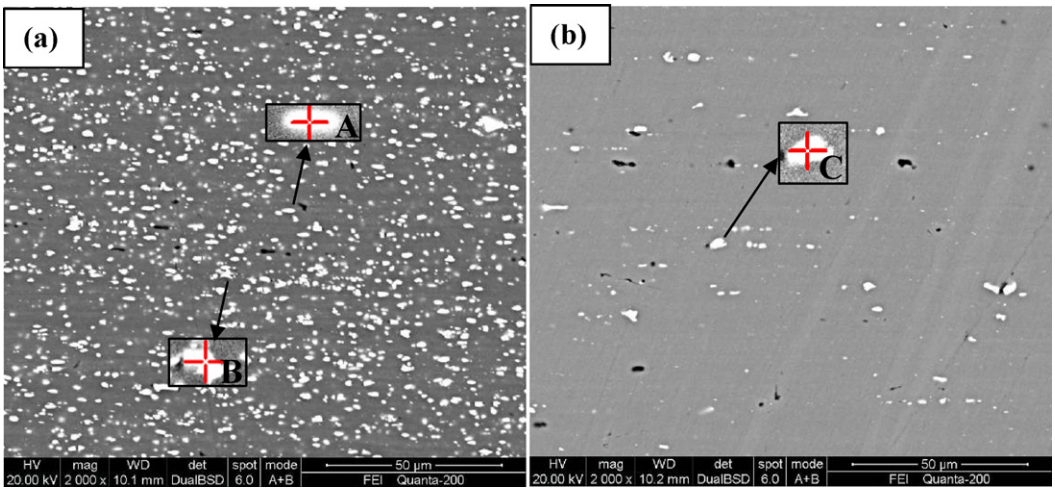

Fig. 9. Back scattered electron images of the alloy under different conditions: (a) cold-rolled and (b) solution treated at 470 °C for 1 h.

Table 2
Chemical composition of the secondary phases in Fig. 9 (in at.%).

Phase	Al	Zn	Mg	Cu	Fe	Si	Mn
A	77.59 ± 2.66	11.58 ± 1.40	9.80 ± 0.47	1.03 ± 0.23	0	0	0
B	82.24 ± 1.18	1.20 ± 0.11	1.39 ± 0.02	0.92 ± 0.17	8.96 ± 0.88	3.45 ± 0.12	1.83 ± 0.08
C	87.36 ± 0.78	1.51 ± 0.21	2.13 ± 0.08	0.42 ± 0.04	4.85 ± 0.51	2.19 ± 0.22	1.53 ± 0.11

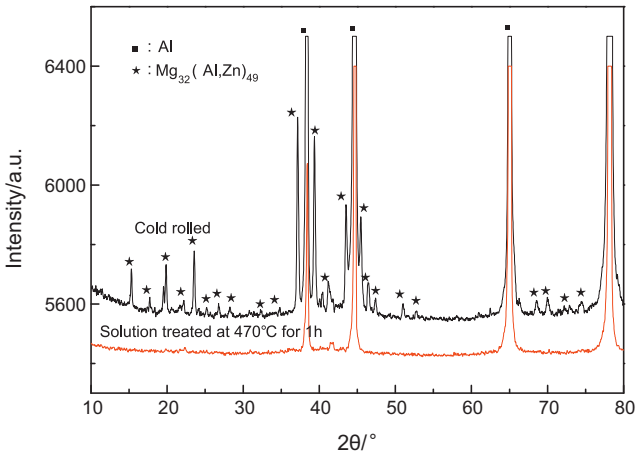

Fig. 10. X-ray diffraction patterns of the sheets under different conditions.

The microstructures of aged alloys were observed by TEM. Fig. 12 shows TEM micrographs of the sheets aged at 120 °C for different durations. Nanometer-sized, spherical $Al_3(Sc, Zr)$ particles can be still observed in grain after aging treatment. In addition, a large number of fine precipitates are distributed homogeneously in matrix (Fig. 12(a)). Those fine precipitates were investigated by high resolution microscopy. High resolution image shown in Fig. 12(b) was taken in $[1\,0\,0]_{Al}$ projection. Fig. 12(b) shows the presence of the GP(I) zones with size ranging from 2 to 8 nm, which is to say that GP zones are the main strengthening precipitates in the alloy under this aging condition (120 °C × 1 h). GP(I) zones are identified according to Refs. [27,28]. They are coherent with Al matrix, with internal ordering of Zn and Al/Mg on the $\{2\,0\,0\}_{Al}$ planes [29,30]. With increasing aging time, GP zones are gradually transferred into η′ and η phases (Fig. 12(c)). After 24 h of aging (peak-aged), the microstructures are still constituent with micro-scaled sub-grains (Fig. 12(d)). Besides, short rod-like particles can be seen in the matrix, and some coarsen rod precipitates are distributed discontinuously along grain boundaries (Fig. 12(e)). The SAD pattern of peak aged sheets in $[1\,1\,2]_{Al}$ projection is shown in Fig. 12(f). The diffraction spots from the aluminum

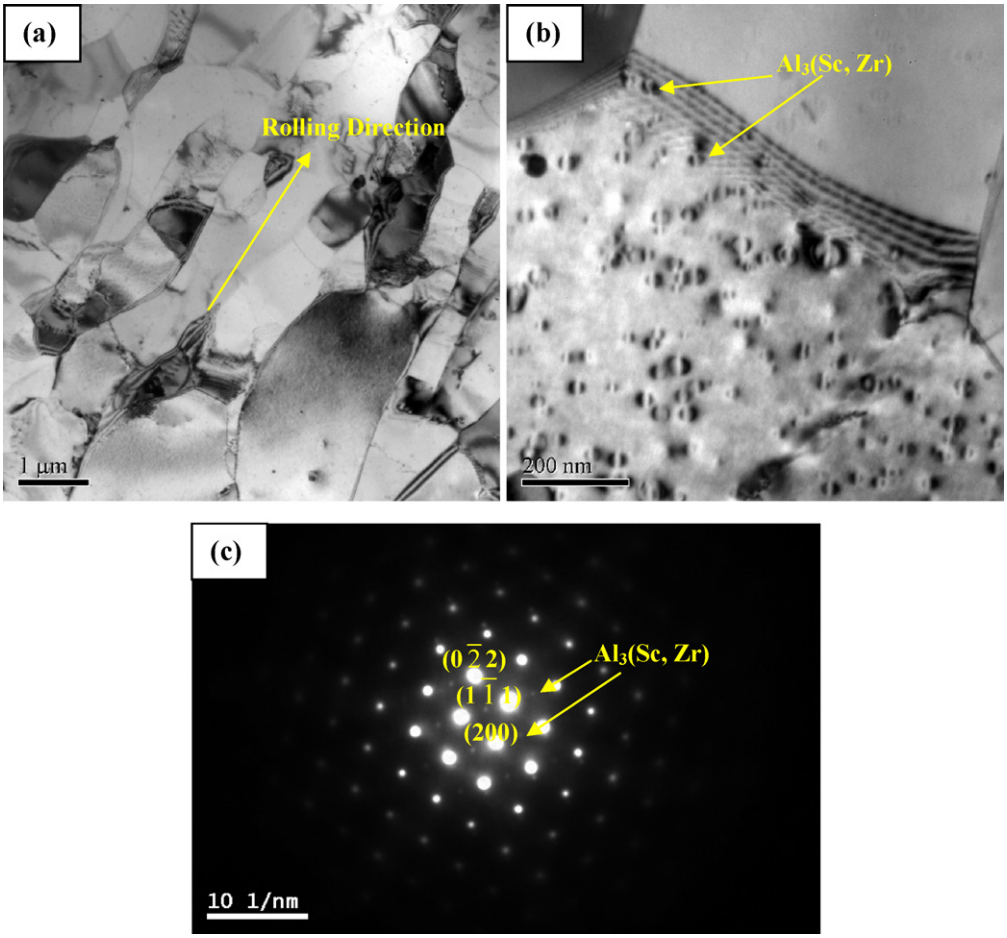

Fig. 11. Microstructures of the alloy after solution treatment at 470 °C for 1 h: (a) Fiber structure with subgrains, (b) $Al_3(Sc, Zr)$ within grains and in sub-grains boundaries, and (c) SAD in $[0\,1\,1]_{Al}$ projection.

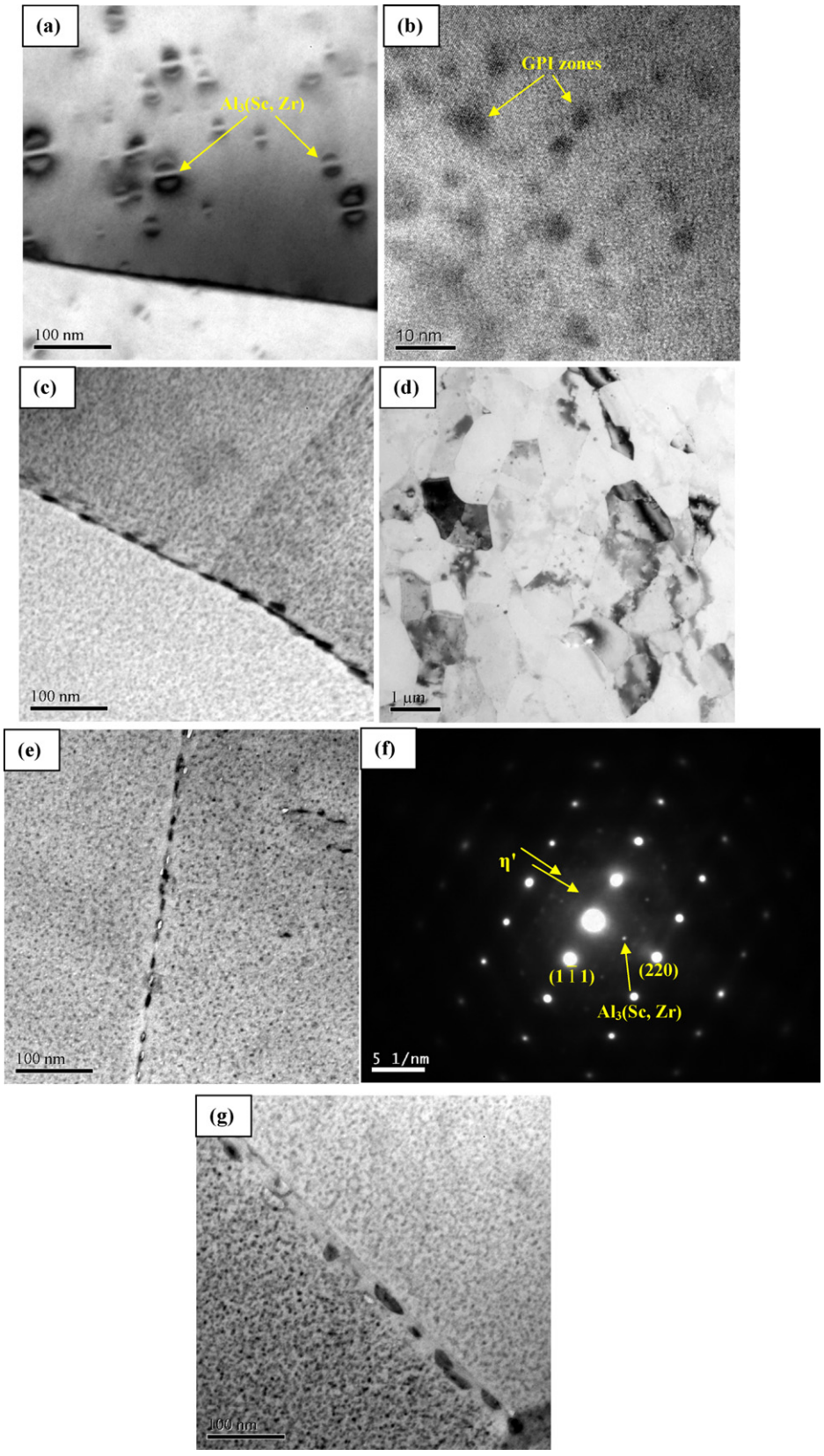

Fig. 12. TEM micrographs of the alloy aged at 120 °C for different duration: (a) 1 h, bright field image; (b) 1 h, HRTEM, $[1\,0\,0]_{Al}$ projection; (c) 12 h, bright field image; (d)–(e) 24 h, bright field image; (f) 24 h, SAD, $[\bar{1}\ 1\ 2]_{Al}$ projection; (g) 36 h, bright field image.

matrix have been indexed. Besides the spots of $Al_3(Sc, Zr)$ particles, there are some spots from η' phase. The η' phase can be identified by referring to the model in some reported results [29,31–33]: (1 0 *l*) and (2 0 *l*) rows in the $[1\,1\,2]_{Al}$ projection, as shown in Fig. 12(f). Therefore, η' phase and $Al_3(Sc, Zr)$ particle are the main strengthening phases in peak-aged alloy. As further prolonging aging time, η' phase coarsens and transfers into η phase (especially in grain boundaries) (Fig. 12(g)), leading to the decrease of strength in sheets as shown in Fig. 8(b).

4. Discussion

4.1. Evolution of microstructures and properties of Al–Zn–Mg–Sc–Zr ingot during homogenization treatment

Under the condition of semi-continuous casting, due to the high cooling rate of melt, the matrix is closest to a supersaturated solid solution. During solidification, owing to the difference of cooling rate between the exterior and center of ingot, eutectic phases formed firstly are pushed into the grain boundaries that are solidified at last. Therefore, lots of Zn and Mg enriched non-equilibrium phases and indissoluble impurity phases containing Fe and Si elements are formed. At the same time, they are concentrated on grain boundaries. Therefore, a homogenization heat treatment is carried out directly after alloy casting, and it plays a key role in removing micro-segregation and dissolving large soluble non-equilibrium eutectic phases formed during solidification. Homogenization temperature and time are two important parameters of homogenization treatment. According to DSC results, we consider that 470 °C is the proper homogenization temperature. With increasing homogenization time at 470 °C, massive non-equilibrium phases gradually dissolve into matrix, leading to increasing the degree of solid solubility of matrix. With the increase of solid solubility, the effect of solution strengthening and the ability of electron scattering are gradually enhanced, causing the gradual increase of hardness and decrease of electrical conductivity of the alloy. After 12 h of homogenizing at 470 °C, dissoluble non-equilibrium phases are primarily dissolved into matrix, resulting in the highest hardness and the lowest electrical conductivity of alloy. As further prolonging homogenization time, the degree of solid solubility of matrix cannot be increased, so there is almost no change of hardness and conductivity.

In addition, the purpose of homogenization heat treatment in the aluminum alloy with Sc and Zr additives is to obtain $Al_3(Sc, Zr)$ particles which is to prevent re-crystallization during hot rolling and solution treatment [23,34,35]. In our studies, massive, fine, nanometer-sized $Al_3(Sc, Zr)$ particles precipitate during homogenization at 470 °C for 12 h. Those particles strongly pin sub-grain boundaries and effectively prevent re-crystallization during subsequent processing and heat treatment, leading micro-scaled sub-grains structures remained in aged sheets. Therefore, the targets of homogenization treatment were achieved after homogenizing at 470 °C for 12 h in our research. As a result, the suitable homogenization treatment is 470 °C × 12 h.

4.2. Evolution of microstructures and properties of Al–Zn–Mg–Sc–Zr sheets during solution-aging treatment

The aim of solution treatment of cold-rolled sheets is to dissolve coarse $T(Mg_{32}(Al,Zn)_{49})$ phase formed during the cooling process of hot rolling into matrix, to improve the degree of super-saturation of alloy which would result in the larger driving force for second phase precipitation during the subsequent aging treatment of sheets. In such case, the matrix can precipitate more second phases during aging treatment, leading to higher strength of aged alloy. Our research shows that aged sheets are obtained lower strength at lower solution temperatures (450 °C or 460 °C) or holding for shorter solution time (0.5 h), owing to that lots of $T(Mg_{32}(Al,Zn)_{49})$ phases still exist in the alloy and the plates are gained lower degree of solid solubility after such solution treatment. At the same time, the grains coarsening and deformed structures disappearing after solution at the higher temperatures (480 °C or 490 °C) or longer duration (1.5 h), also cause the lower strength of aged alloy. As a whole, after solution treatment at 470 °C for 1 h, coarse $T(Mg_{32}(Al,Zn)_{49})$ phases primarily dissolve to matrix, the deformed structures are remained in the sheets and the aged sheets have better tensile properties. Therefore, the suitable solution treatment is 470 °C × 1 h.

In the 7xxx series Al alloys the supersaturated solid-solution decomposes in the following sequence [36–40]: Supersaturated solid-solution (α) → GP zones → η' ($MgZn_2$) → η ($MgZn_2$). The η' phase is one of the most important age-hardening precipitate in commercial Al–Zn–Mg alloys. When the aging time is too long or the aging temperature is too high, metastable η' phase will transform into stable η phase, achieving over-aging. Observed from Fig. 8, the studied sheets are in peak-aged T6 state at 120 °C for 24 h. Aged at 120 °C, with increasing aging time, the precipitates gradually transform from coherent GP zones to semi-coherent η' phase, and then incoherent η phase, corresponding to a typical behavior of aging strengthening, as shown in Fig. 8(b). In addition, $Al_3(Sc, Zr)$ particles do not change the characteristic of aging precipitation during aging treatment in studied alloy. Therefore, the optimized aging treatment of studied sheets is 120 °C × 24 h.

Furthermore, from the observation of the microstructures in T6 state sheets (120 °C × 24 h), the grain structures are composed of micro-scaled sub-grains, and the main phases are η' precipitates and $Al_3(Sc, Zr)$ particles. Therefore, the main strengthening mechanisms of Al–Zn–Mg–Sc–Zr aged sheets are precipitation strengthening of η' precipitates, and dispersion strengthening and sub-grain strengthening caused by coherent $Al_3(Sc, Zr)$ particles.

5. Conclusions

Under the condition of semi-continuous casting, the matrix is closest to a supersaturated solid solution. Lots of Zn and Mg enriched non-equilibrium phases and indissoluble impurity phases containing Fe and Si elements are concentrated on grain boundaries. Therefore, the homogenization treatment is required to eliminate severe segregation in the as-cast alloy.

After homogenization treatment, Zn and Mg enriched non-equilibrium phases are dissolved into matrix. At the same time, supersaturated solid solution decomposes and dispersed, nanometer-sized $Al_3(Sc, Zr)$ particles precipitate. The suitable homogenization treatment of Al–Zn–Mg–Sc–Zr alloy is 470 °C × 12 h.

The suitable solution-aging treatment of Al–Zn–Mg–Sc–Zr sheets with thickness of 2 mm is solution treated at 470 °C for 1 h, followed by water quenching and then aged at 120 °C for 24 h. Under this condition, the tensile strength, yield strength and elongation of the sheets reach 555 ± 2 MPa, 524 ± 4 MPa and 12.3 ± 0.6% respectively.

The main strengthening mechanisms of Al–Zn–Mg–Sc–Zr aged sheets are precipitation strengthening derived from η' precipitates, and dispersion strengthening and sub-grain strengthening caused by coherent $Al_3(Sc, Zr)$ particles.

Acknowledgments

This work was financially supported by the National Civilian Matched Project of China (JPPT-115-2-948), the National General Pre-research Project of China (51312010402), Hunan Provincial

Innovation Foundation for Postgraduate (CX2011B111) and the Graduate Degree Thesis Innovation Foundation of Central South University (2011ybjz014).

References

[1] S.K. Panigrahi, R. Jayaganthan, J. Alloys Compd. 509 (2011) 9609–9616.
[2] C.M. Cepeda-Jiménez, J.M. García-Infanta, O.A. Ruano, F. Carreño, J. Alloys Compd. 509 (2011) 9589–9597.
[3] A. Kverneland, V. Hansen, G. Thorkildsen, H.B. Larsen, P. Pattison, X.Z. Li, J.Gjønnes, Mater. Sci. Eng. A 528 (2011) 880–887.
[4] R.K.R. Singh, C. Sharma, D.K. Dwivedi, N.K. Mehta, P. Kumar, Mater. Des. 32 (2011) 682–687.
[5] N.M. Han, X.M. Zhang, S.D. Liu, D.G. He, R. Zhang, J. Alloys Compd. 509 (2011) 4138–4145.
[6] B. Li, H.W. Wang, J.C. Jie, Z.J. Wei, Mater. Des. 32 (2011) 1617–1622.
[7] X.M. Li, M.J. Starink, J. Alloys Compd. 509 (2011) 471–476.
[8] L. Lityńska-Dobrzyńska, J. Dutkiewicz, W. Maziarz, A. Góral, J. Alloys Compd. 509S (2011) S304–S308.
[9] T.V. Atamanenko, D.G. Eskin, M. Sluiter, L. Katgerman, J. Alloys Compd. 509 (2011) 57–60.
[10] B. Li, H.W. Wang, J.C. Jie, Z.J. Wei, J. Alloys Compd. 509 (2011) 3387–3392.
[11] C. Monachon, M.E. Krug, D.N. Seidman, D.C. Dunand, Acta Mater. 59 (2011) 3398–3409.
[12] W.T. Wang, X.M. Zhang, Z.G. Gao, Y.Z. Jia, L.Y. Ye, D.W. Zheng, L. Liu, J. Alloys Compd. 491 (2010) 366–371.
[13] W.H Yuan, Z.Y Liang, Mater. Des. 32 (2011) 4195–4200.
[14] X. Chen, Z.Y. Liu, S. Bai, Y. Li, L.H Lin, J. Alloys Compd. 505 (2010) 201–205.
[15] A.K. Mukhopadhyay, A. Kumar, S. Raveendra, I. Samajdar, Scr. Mater. 64 (2011) 386–389.
[16] B.A. Chen, L. Pan, R.H. Wang, G. Liu, P.M. Cheng, L. Xiao, J. Sun, Mater. Sci. Eng. A 530 (2011) 607–617.
[17] K.E. Knipling, R.A. Karnesky, C.P. Lee, D.C. Dunand, D.N. Seidman, Acta Mater. 58 (2010) 5184–5195.
[18] K.E. Knipling, D.N. Seidman, D.C. Dunand, Acta Mater. 59 (2011) 943–954.
[19] M.E. van Dalen, T. Gyger, D.C. Dunand, D.N. Seidman, Acta Mater. 59 (2011) 7615–7626.
[20] C. Booth-Morrison, D.C. Dunand, DaN. Seidman, Acta Mater. 59 (2011) 7029–7042.
[21] L.M. Wu, W.H. Wang, Y.F. Hsub, S. Trong, J. Alloys Compd. 456 (2008) 163–169.
[22] O.N. Senkov, M.R. Shagiev, S.V. Senkova, D.B. Miracle, Acta Mater. 56 (2008) 3723–3738.
[23] V.G. Davydov, V.I. Elagin, V.V. Zakharov, T.D. Rostova, Met. Sci. Heat Treat. 38 (1996) 347–350.
[24] L.M. Wu, M. Seyring, M. Rettenmayr, W.H. Wang, Mater. Sci. Eng. A 527 (2010) 1068–1073.
[25] C.B. Fuller, D.N. Seidman, Acta Mater. 53 (2005) 5415–5428.
[26] W. Lefebvre, F. Danoix, H. Hallem, B. Forbord, A. Bostel, K. Marthinsen, J. Alloys Compd. 470 (2009) 107–110.
[27] L.K. Berg, J. Gjønnes, V. Hansen, X.Z. Li, M. Knutson-wedel, G. Waterloo, D. Wallenberg, Acta Mater. 49 (2001) 3443–3451.
[28] K. Stiller, P.J. Warren, V. Hansen, J. Angenete, J. Gjønnes, Mater. Sci. Eng. A 270 (1999) 55–63.
[29] Z.H. Li, B.Q. Xiong, Y.G. Zhang, B.H. Zhu, F. Wang, H.W. Liu, Mater. Charact. 59 (2008) 278–282.
[30] C.B. Fuller, M.W. Mahoney, M. Calabrese, L. Micona, Mater. Sci. Eng. A 527 (2010) 2233–2240.
[31] X.Z. Li, V. Hansen, J. Gjønnes, L.R. Wallenberg, Acta Mater. 47 (1999) 2651–2659.
[32] Z.W. Du, Z.M. Sun, B.L. Shao, T.T. Zhou, C.Q. Chen, Mater. Charact. 56 (2006) 121–128.
[33] P.C. Bai, T.T. Zhou, P.Y. Liu, Y.G. Zhang, C.Q. Chen, Mater. Lett. 58 (2004) 3084–3087.
[34] Z.H. Jia, G.Q. Hu, B. Forbord, J. Ketil Solberg, Mater. Sci. Eng. A 444 (2007) 284–290.
[35] V. Singh, K. Satya Prasad, A.A. Gokhale, Scr. Mater. 50 (2004) 903–908.
[36] M. Liu, B. Klobes, K. Maier, Scr. Mater. 64 (2011) 21–24.
[37] G. Waterloo, V. Hansen, J. Gjønnes, S.R. Skjervold, Mater. Sci. Eng. A 303 (2001) 226–233.
[38] C. Wolverton, Acta Mater. 49 (2001) 3129–3142.
[39] B.C. Wei, C.Q. Chen, Z. Huang, Y.G. Zhang, Mater. Sci. Eng. A 280 (2000) 161–167.
[40] M.J. Starink, S.C. Wang, Acta Mater. 51 (2003) 5131–5150.